Tailoring Magnetic Properties of Cubic Spinel Ferrite Core–Shell Nanoparticles for Magnetoresistive Engineering

M. Kuźmiński[a,*], A. Belous[b], O. Yelenich[b], S. Solopan[b], K.M. Kosyl[a], A.N. Fitch[c], W. Paszkowicz[a], P. Dłużewski[a], A. Kaleta[a], N. Nedelko[a] and A. Ślawska-Waniewska[a]

[a]*Institute of Physics, Polish Academy of Sciences, al. Lotników 32/46, PL-02668 Warsaw, Poland*
[b]*V.I. Vernadskii Institute of General and Inorganic Chemistry, 32/34 Palladina Avenue, 03680 Kyiv, Ukraine*
[c]*European Synchrotron Radiation Facility (ESRF), BP 220, F-38043 Grenoble, France*

Received: 09.05.2025 & Accepted: 25.06.2025

Doi: 10.12693/APhysPolA.148.12 *e-mail: kuzmi@ifpan.edu.pl

Magnetite nanoparticles with a cobalt ferrite shell provide the opportunity to obtain a tunneling magnetoresistance structure and offer an additional degree of freedom in shaping the magnetoresistive characteristics. In order to investigate the effect of the relative fractions of the shell on magnetic and magnetoresistive properties, we have prepared (by chemical co-precipitation) a bi-magnetic (soft/hard) core–shell $Fe_3O_4/CoFe_2O_4$ nanoparticle system (with diameters of a few nm). The structural, magnetic, and electric transport properties of the as-prepared core precursor, core–shell nanoparticles, and sintered powder were determined. It was found that the obtained particles, which are few nanometers in size, have the desired single-crystalline spinel structure with a core–shell architecture and the expected magnetic properties associated with core–shell interactions. Sintering leads to more complex magnetic behavior and tunneling conductance.

topics: ferrites, nanoparticles, magnetic properties, electrical properties

1. Introduction

The creation of complex architectures at the nanometer scale allows new properties to be achieved. Magnetic nanostructures have aroused great interest, pushing the boundaries of magnetic information storage technology, as well as enhancing the understanding of spin-dependent transport phenomena. Spin-dependent transport has attracted much attention since the discovery of giant magnetoresistance (GMR), colossal magnetoresistance [1, 2], and tunneling magnetoresistance (TMR) in so-called magnetic tunnel junctions (MTJs) [3, 4]. The TMR is especially attractive because the values of magnetoresistance obtained in MTJs greatly surpassed those of the GMR [5]. In addition, MTJ devices are highly versatile, allowing the combination of electrodes and barriers of various types [6–8].

However, it is difficult to obtain high spin polarization values of electric current and improve the TMR effect using classical ferromagnetic transition metals. The search for materials with high spin polarization has focused (among others) on a family of materials known as half-metals [9–11], such as magnetite (Fe_3O_4) or other magnetic oxides. Significant TMR — sometimes called "powder magnetoresistance" effects (PMR) — has been reported in compacted powder pellets of materials with high spin polarization [12–14]. In both TMR and PMR, a thin non-magnetic layer on the grain surfaces plays the role of a barrier for the spin-polarized electrons [12, 13, 15, 16]. For this form of microstructure, in the ideal case, each magnetic grain boundary can be a spin-selecting junction, and the total number of junctions increases by many orders of magnitude [17–19].

Characteristic feature of TMR/PMR systems is that the plot of the resistance vs applied external magnetic field (H) usually has a maximum at the field ($H^{\mathrm{MR}}_{\mathrm{max}}$) equal (or very close) to the coercive field (H_c) of the total magnetization (M) [12, 13, 15]. However, it could be of interest to have the freedom to shape the magnetoresistive characteristic, i.e., to obtain quasi-independent magnetic and magnetoresistive (MR) responses to the applied magnetic field.

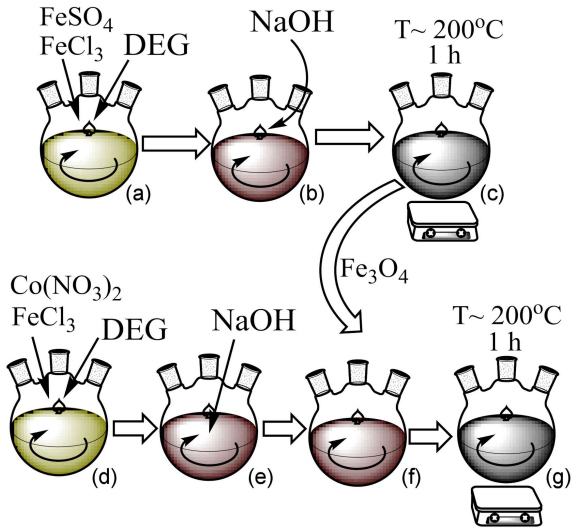

Fig. 1. Schematic presentation of the synthesis procedures for ferrimagnetic nanoparticles.

Such an possibility has been discovered in Sr_2FeMoO_6 powder [20–22], where the MR peak was observed at H_{max}^{MR} that was many times higher than H_c. This shows a way to intentionally manipulate the tunneling process through controlled creation of an appropriate insulating magnetic barrier, whose spin orientation relative to that of the metallic grain can be controlled by the application of a suitable magnetic field intensity. This possibility is provided by bi-magnetic core–shell nanoparticles composed of ferrites that differ in terms of electrical conductivity and magnetic anisotropy [23–29].

Research into nano-sized magnets, known as "magnetic nanoparticles", began with the advent of nanotechnology [30]. Advances in chemical synthetic methods offer an affordable route for the "bottom-up" synthesis of complex nanostructures, with precise control over their chemical composition, shape, and size. New composite nano-ferrites (as core–shell nanoparticles) are the subject of intensive research due to their numerous possible applications [31–33]. Improved synthesis methods enable re-examination of the feasibility of granular magnetoresistance (multiple tunnel junctions) via a bottom-up nanochemical approach [19].

In the case of ferrite core–shell (bi-magnetic) nanoparticles, the tunneling magnetoresistance may depend on the particle sizes and relative fractions of the constituent core and shell materials. Thus, the present work is motivated by the authors' interest in understanding the extent to which these nanostructure parameters affect the MR properties and the relative behavior of H_c and H_{max}^{MR}. For these studies (which are complementary to those previously published [23]), we prepared $Fe_3O_4/CoFe_2O_4$ core–shell nanoparticles to check the effect of increasing the ratio of the $CoFe_2O_4$ shell volume to core volume.

Both ferrites forming the nanoparticle have a cubic spinel structure. In the bulk form, Fe_3O_4 (magnetite) is a magnetically soft ferrimagnet with a Curie temperature of $T_C \simeq 860$ K, high specific magnetization, and coercivity of a few Oe at room temperature. In turn, cobalt ferrite ($CoFe_2O_4$) is magnetically hard, with a much higher value of the magnetocrystalline anisotropy constant. These ferrites also differ in terms of electric conductivity, namely magnetite is considered a "poor metal" because its resistivity is slightly too high to be classified as a metal, whereas $CoFe_2O_4$ is a regular insulator at room temperature [34].

It should be emphasized that the nanoparticles prepared for resistivity measurements are not coated with any organic spacer typically used to prevent agglomeration. In this paper, the sample preparation, structural characterization (including attempts to distinguish the $CoFe_2O_4$ shell on the basis of transmission electron microscopy (TEM) or synchrotron X-ray analysis), as well as basic magnetic and electric transport properties are presented.

2. Materials and methods

Bi-magnetic spinel ferrite core–shell nanoparticles comprising magnetic hard ($CoFe_2O_4$) and soft phases (Fe_3O_4) were synthesized by a combination of hydrolysis of coordination compounds in a high-temperature organic solvent with a seed-mediated growth process according to synthesis procedures reported in [35]. As reactants, iron(III) chloride nonahydrate (97% $FeCl_3 \cdot 9H_2O$), cobalt(II) nitrate hexahydrate (98% $Co(NO_3)_2 \cdot 6H_2O$), iron(II) sulfate heptahydrate (99% $FeSO_4 \cdot 7H_2O$), sodium hydroxide (98% NaOH), and diethylene glycol (99% DEG) purchased from Sigma-Aldrich were used.

2.1. Synthesis of Fe_3O_4 nanoparticles

For the synthesis of Fe_3O_4 nanoparticles, the $FeSO_4 \cdot 7H_2O$ and $FeCl_3 \cdot 9H_2O$ salt solutions in a 1:2 molar ratio were mixed with diethylene glycol in a three-neck flask under a flowing argon atmosphere (Fig. 1a). At the same time, a NaOH alkali solution in DEG was prepared, added drop by drop to the solution of salts ($FeSO_4 \cdot 7H_2O$ and $FeCl_3 \cdot 9H_2O$), and stirred for 2 h (Fig. 1b). The resulting mixture was heat-treated at 200–220°C for 60 min (Fig. 1c). Oleic acid was then added to the diethylene glycol solution, and the mixture was stirred for 20 min. After cooling, the resulting nanoparticles were centrifuged, washed with an ethanol–water solution, and dried in open air at 50°C for 10 h.

2.2. Synthesis of $Fe_3O_4/CoFe_2O_4$ nanoparticles

$Fe_3O_4/CoFe_2O_4$ nanoparticles with a core–shell architecture were synthesized in a three-neck flask under a flowing argon atmosphere. First, $Co(NO_3)_2 \cdot 6H_2O$ and $FeCl_3 \cdot 9H_2O$ solutions were mixed with DEG, and the mixture was stirred for 20 min (Fig. 1d). At the same time, NaOH in DEG was prepared and added to the mixture of the salts $Co(NO_3)_2 \cdot 6H_2O$ and $FeCl_3 \cdot 9H_2O$ (Fig. 1e). After 2 h of stirring, the Fe_3O_4 nanoparticles (in DEG), synthesized by the method described above (see Fe_3O_4 preparation) without the oleic acid addition procedure, were introduced to the reaction medium (Fig. 1f). The resulting solution was heat-treated at 200–220°C C for 90 min (Fig. 1g). After cooling, the resulting nanoparticles were centrifuged, washed with an ethanol–water solution, and dried in open air at 50°C for 10 h.

It should be noted that, in contrast to the typical (final) procedure described in other studies on similar nanoparticles, the obtained nanoparticles (prepared mainly for resistivity measurements) are not coated with oleic acid or any other organic separator.

2.3. Pellet preparation

Portions of the obtained powder ($\simeq$ 100 mg) were cold pressed (axial pressure $\simeq$ 400 MPa) in a 5 mm diameter steel die into discs/pellets $\simeq$ 1 mm in thickness and then annealed (sintered) in argon gas at 450°C for 2 h in order to improve interparticle mechanical and electrical connections (which probably result in partial fusing of their shells). These conditions reduce the contact resistance, maintaining interdiffusion between core and shell insufficient to degrade the core–shell structure [23].

2.4. Characterization techniques

High-resolution powder X-ray diffraction for all the samples was performed on the ID22 beamline at the European Synchrotron Radiation Facility (ESRF) in Grenoble. The used wavelength was $\lambda = 0.354575(6)$ Å. The applied diffraction geometry involving analyzer crystals allows for an extremely small instrumental contribution to the peak full width at half maximum (ca. 0.003° of 2θ). The structure refinements, employing the Rietveld method, were performed using TOPAS 5 software. The microstructure of the as-prepared nanoparticles was additionally characterized by transmission electron microscopy (TEM), using an image-corrected Titan Cubed 80-300 microscope operating at 300 kV. Elemental composition was analyzed by energy-dispersive X-ray spectroscopy (EDX) performed during TEM measurements, employing an EDAX 30 mm^2 Si(Li) detector with a collection angle of 0.13 sr. Magnetic properties (of powder and pellets) and magnetoresistance (of pellets) were studied using the Physical Property Measurement System (PPMS) from Quantum Design, equipped with the Vibrating Sample Magnetometer (VSM) option or, alternatively, the Resistivity option. Magnetic measurements were performed in the temperature range of 2–390 K and a field range of ±9 T. For the resistivity measurements, electrical leads were attached to the pellets on the holder (puck) with silver paint. Additionally, the Keithley Model 2400 SourceMeter was used in the cases of very high resistances (dozens of GΩ) at the lowest temperatures.

3. Results and discussion

3.1. Structure

The collected high-resolution synchrotron X-ray powder diffractograms are presented in Fig. 2. All the diffractograms confirm the obtainment of the desired spinel ($MgAl_2O_4$) structure, with the refined lattice parameters quoted in Table I (including reference data [36–38]). The refinement gives a = 8.370(2), 8.391(1), and 8.3839(3) Å for samples of Fe_3O_4, $Fe_3O_4/CoFe_2O_4$ nanoparticles, and the annealed pellet of compacted $Fe_3O_4/CoFe_2O_4$, respectively.

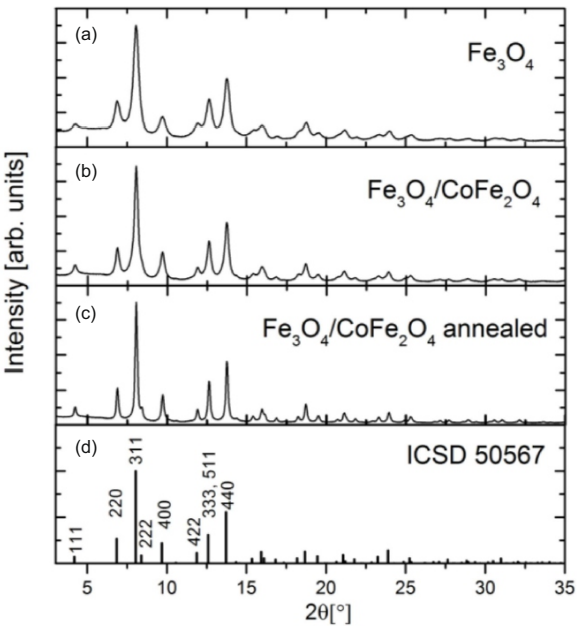

Fig. 2. X-ray diffractograms of (a) Fe_3O_4 core, (b) $Fe_3O_4/CoFe_2O_4$ core–shell, and (c) annealed core–shell nano-powders. (d) A powder XRD pattern of Fe_3O_4 (spinel) comes from the ICSD database 2025.

TABLE I

Lattice parameters (for Fe_3O_4 nanoparticles, $Fe_3O_4/CoFe_2O_4$ core–shell nanoparticles, and annealed pellet of compacted $Fe_3O_4/CoFe_2O_4$) obtained using the Rietveld procedure compared with reference data [ICSD]. Here, R_{wp} is the weighted profile residual factor.

Sample/material	Refinement results		Reference (bulk material)	
	a [Å]	R_{wp} [%]	a [Å]	Source
Fe_3O_4	8.370(2)	6.5	8.3967(3)	Bosi et al. [36]
$Fe_3O_4/CoFe_2O_4$	8.391(1)	6.1	–	–
$Fe_3O_4/CoFe_2O_4$ annealed	8.3839(3)	4.5	–	–
Fe_2O_3	–	–	8.3457	Shin [37]
$CoFe_2O_4$	–	–	8.3806(1)	Ferreira et al. [38]

Diffraction peaks, in the case of non-annealed samples, are strongly broadened, which is due to the nanometer size of the crystallites (the instrumental effect is negligible because of the high-resolution setup). In order to estimate the particle sizes, the Scherrer equation was applied (to the data of 440 reflection), resulting in the following crystallite sizes: 4.3, 6.0, and 10.9 nm for Fe_3O_4, $Fe_3O_4/CoFe_2O_4$ nanoparticles, and annealed $Fe_3O_4/CoFe_2O_4$ nanoparticles, respectively. The quite good agreement of the obtained crystallite sizes for $Fe_3O_4/CoFe_2O_4$ with the electron microscopy results (presented below) indicates that the nano-powder consists of single-crystalline particles. Additionally, the above crystal size estimate for core–shell nanoparticles is considerably greater than that for the Fe_3O_4 nanoparticles, providing an argument for the existence of a $CoFe_2O_4$ shell on the Fe_3O_4 core.

In the case of as-prepared (non-annealed) samples, a peak shape asymmetry was observed (see example in Fig. 3), with a possible origin in the non-homogeneity of the sample. The instrumental contribution can be excluded in this case, as the asymmetry is well visible not only in the low-angle part of the diffractograms. The presence of this peak asymmetry in the case of both homogeneous and core–shell nanoparticles indicates that the origin of this asymmetry is not necessarily connected to the existence of the $CoFe_2O_4$ shell (and its slightly different lattice constant). On the other hand, alterations in the lattice constant (within the depth of Fe_3O_4 nanoparticles), caused by possible oxidation to maghemite [34, 39] on the particle surface (or a stoichiometric gradient in the nanoparticle), can cause a similar effect. It is also worth mentioning the supposed presence of some amount of amorphous content in the non-annealed (as-prepared) materials, manifesting itself through broad (low-intensity) humps of similar q-values and shape to those presented in [39]. This pattern feature was not pronounced in the annealed sample, leading to the conclusion that at least some part of the amorphous content had crystallized.

The refined lattice parameters fall between the Fe_3O_4 (8.3967 Å) and γ-Fe_2O_3 (8.3457 Å) bulk

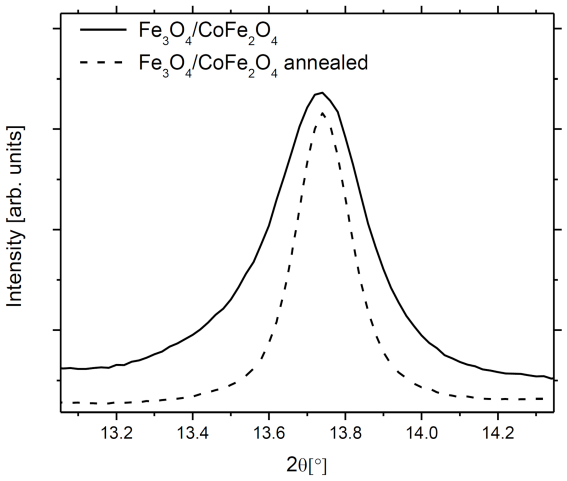

Fig. 3. The 440 reflections in the case of as-prepared and annealed $Fe_3O_4/CoFe_2O_4$ core–shell nanoparticles (enlargement of a fragment of Fig. 2). In the case of the as-prepared sample, the aforementioned asymmetry of the 440 reflection is observed.

reference data [ICSD database, 2025]. Competing effects should be taken into account: (i) lattice contraction as a result of surface oxidation (to maghemite) and (ii) lattice expansion caused by surface relaxation [39], especially for the smallest particles [40]. The Fe_3O_4 sample lattice parameter is near the arithmetical middle (of the mentioned reference data), probably because of some maghemite surface layer [34, 39]. For $Fe_3O_4/CoFe_2O_4$ nanoparticles, this parameter is between Fe_3O_4 and $CoFe_2O_4$ bulk data, probably because of lesser oxidation (which may be the result of the protective role of the $CoFe_2O_4$ layer and generally larger particles). In addition, oxidation can vary significantly from sample to sample, depending on the preparation and storage [39]. A smaller lattice parameter after annealing may be caused by weaker surface relaxation for larger particles [40].

As regards the significant increase in the estimated nano-crystallite size after annealing (from 6.0 to 10.9 nm), it may be partly explained by the generally higher crystallinity index (as a result of the

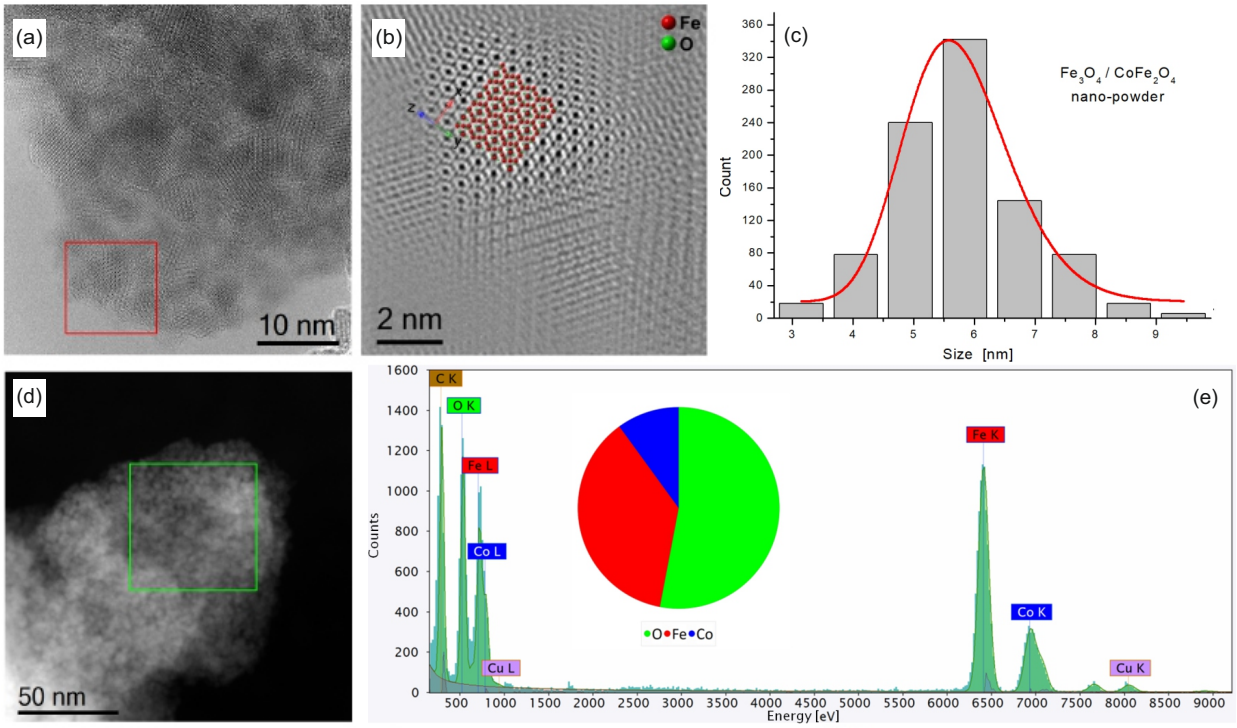

Fig. 4. (a) High-resolution TEM image of as-prepared $Fe_3O_4/CoFe_2O_4$ nanoparticles. (b) Magnified view of the region marked by the red square in panel (a), processed by Fourier filtering, presenting a particle oriented along the [011] zone axis. A model of the Fe_3O_4 crystal structure is superimposed on the high-resolution image. (c) Particle size distribution obtained from TEM images, fitted with a lognormal function. (d) STEM-HAADF image of the nanoparticle agglomerates. (e) Integrated EDX spectrum, collected from the area indicated by the green square in panel (d), revealing an O:Fe:Co atomic percent ratio of approximately 53:37:10 (shown in the color-coded chart).

reduction of the amorphous phase and the homogenization of the nanoparticles). However, the real size increase (coarsening) and the joining of nanoparticles contribute as well.

Figure 4a shows the high-resolution transmission electron microscopy (TEM) image of as-prepared $Fe_3O_4/CoFe_2O_4$ nanoparticles. Due to their identical crystallographic structures and minimal lattice mismatch, semi-epitaxial growth of the $CoFe_2O_4$ shell over the Fe_3O_4 core is possible, as previously reported in the literature [41, 42]. As a result, the core–shell architecture is not distinctly visible in the image. Thus, the thickness of the cobalt ferrite shell was estimated to be ~ 1 nm, based on the size difference between the core–shell and uncovered Fe_3O_4 particles. A Fourier-filtered magnified area (highlighted by the red square in Fig. 4a) is shown in Fig. 4b, revealing a well-oriented particle. The Fe_3O_4 crystal structure was identified by measuring two interplanar spacings and the angle between them. Consequently, the [011] zone axis projection of the Fe_3O_4 structure was superimposed on the high-resolution image and showed excellent agreement with the observed pattern. Particle size analysis based on TEM images indicates that the particles are nearly monodisperse with a relatively narrow size distribution, as presented in Fig. 4c. Fitting the data with a lognormal function gives an average particle diameter of 5.8 nm with a standard deviation of 0.9 nm.

Moreover, energy-dispersive X-ray spectroscopy (EDX) was performed using scanning transmission electron microscopy (STEM) and a high-angle annular dark field (HAADF) detector. The EDX signal collected from an agglomeration of particles (shown in Fig. 4d) is presented in Fig. 4e and reveals an atomic percent of Fe : O : Co = 37 : 53 : 10. This composition confirms the proposed structure of Fe_3O_4 cores coated with ≈ 1 nm thick $CoFe_2O_4$ shells.

The TEM results are consistent with those of the complementary X-ray analysis, despite certain differences between the estimation methods. From the TEM images, we obtained a "number-based" size distribution (and average) of particle diameter values [39].

Structural studies have shown that the obtained (as-prepared) few-nanometer-sized particles have the desired spinel structure. The complementary X-ray, EDX, and TEM results show that, in the case of core–shell particles, the Fe_3O_4 core with a spinel structure is covered by a $CoFe_2O_4$ shell. Furthermore, TEM results indicate a relatively narrow size distribution.

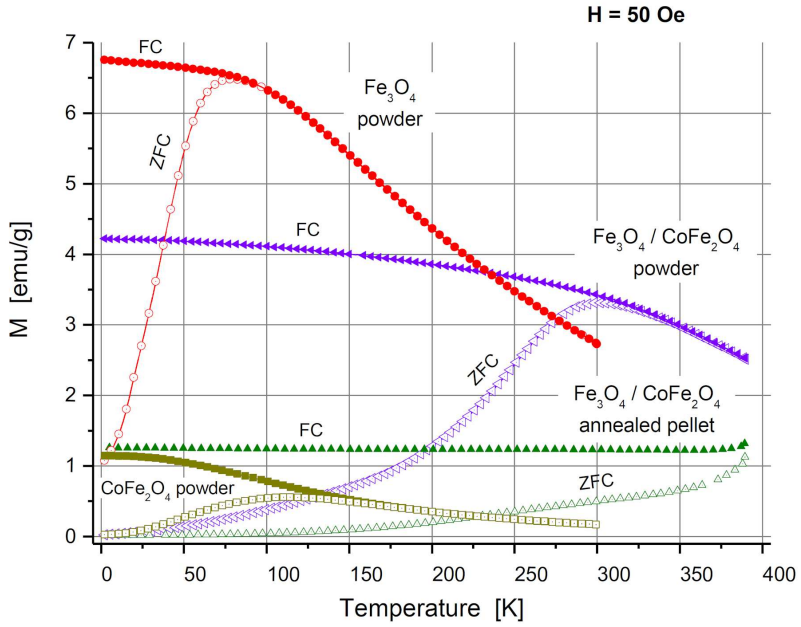

Fig. 5. Temperature dependences (2–390 K) of the zero-field-cooled (ZFC) and field-cooled (FC) magnetization measured for the core–shell $Fe_3O_4/CoFe_2O_4$ nanoparticles (◁), compacted and annealed pellets (△), and uncovered Fe_3O_4 particles (◯). The dependences for as-prepared $CoFe_2O_4$ particles (□) with diameters similar to those of Fe_3O_4 particles are presented for comparison[†1].

3.2. Magnetic properties

As seen from the thermal dependence of the field-cooled (FC) magnetization (measured in an external field of 50 Oe) for as-prepared $Fe_3O_4/CoFe_2O_4$ nanoparticles, the magnetization decreases monotonically with increasing temperature, whereas the zero-field-cooled (ZFC) curve displays a maximum with the peak temperature equal to ~ 300 K, which is much higher than the one (~ 80 K) observed for uncovered Fe_3O_4 particles — see Fig. 5. If we approximately consider observed peak temperatures as the average blocking temperatures for superparamagnetic relaxations $\langle T_B \rangle$, then such a huge enhancement of the peak temperature can be related to the increase in the effective anisotropy of particles which originates from magnetically hard $CoFe_2O_4$ shells. This fact, along with the single maximum ("blocking temperature") observed for $Fe_3O_4/CoFe_2O_4$ nanoparticles, can be interpreted as a confirmation of the efficient core–shell exchange coupling. It should be noted, however, that although the samples described are in the form of loosely compacted powder, the shape of ZFC–FC curves and the obtained T_B values may not represent the properties of ideal, isolated superparamagnetic nanoparticles. The differences may be due to long-range magnetostatic interactions between particles and the lack of an insulating organic shell on the particles. Additionally, the surface of the nanoparticles has a significant contribution at the nanoscale due to the large surface-to-volume ratio. Since the surface of the nanoparticles has a higher concentration of vacancies, disorders, and broken bonds compared to the core, the surface ordering under the influence of the magnetic field can be very different [33, 43, 44].

In the case of strongly compacted and annealed pellets, the ZFC and FC curves (also shown in Fig. 5) do not coincide, and no maximum is observed in the ZFC curve in the available temperature range because of stronger interparticle coupling, as well as possible microstructural changes occurring at interfaces during annealing. The dependences for as-prepared $CoFe_2O_4$ particles with diameters similar to those of Fe_3O_4 particles are also presented (in Fig. 5) for comparison[†1].

Magnetization hysteresis loops, $M(H)$, measured at different temperatures (2–300 K) for as-prepared powder and annealed pellets are presented in Fig. 6a and b, respectively. The uncoated Fe_3O_4 particles at 2 K exhibit the magnetization curve typical of a soft magnet, with a coercivity of around 300 Oe. For $Fe_3O_4/CoFe_2O_4$ powder, the coercivity increases $\approx$ 20 times, reflecting the increase in the total anisotropy of heterostructured particles. This result can be explained by the large contribution of

[†1] Supplementary results concern $CoFe_2O_4$ nanoparticle powder, which was prepared using the same procedure as for the other particles studied in this work. The conditions were selected to obtain particles with diameters similar to those of Fe_3O_4 particles.

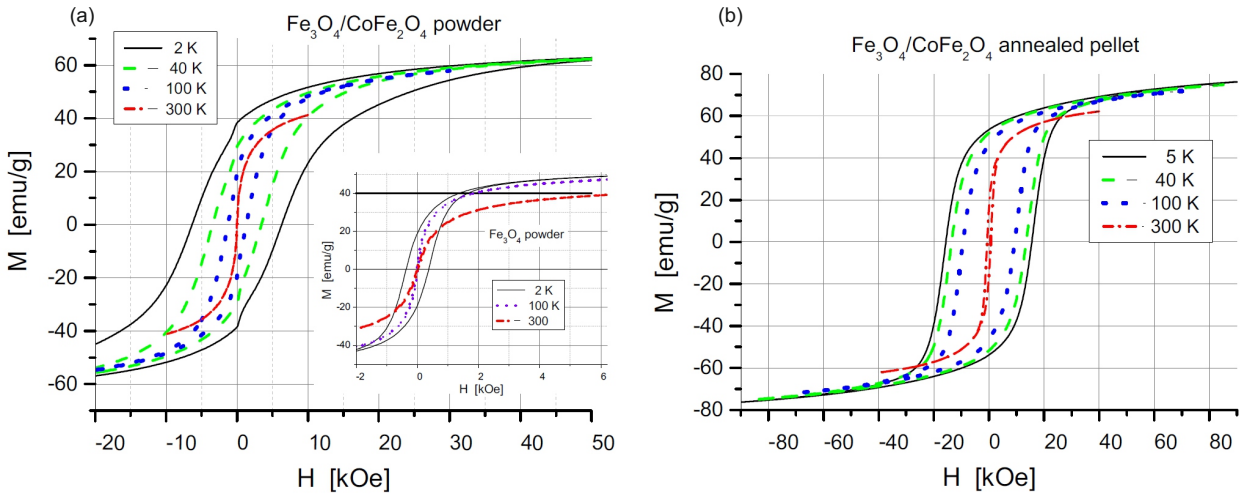

Fig. 6. Magnetization hysteresis loops, $M(H)$, measured at different temperatures for as-prepared $Fe_3O_4/CoFe_2O_4$ powder (a) and annealed pellet (b). The inset shows the hysteresis loops for as-prepared Fe_3O_4 particles.

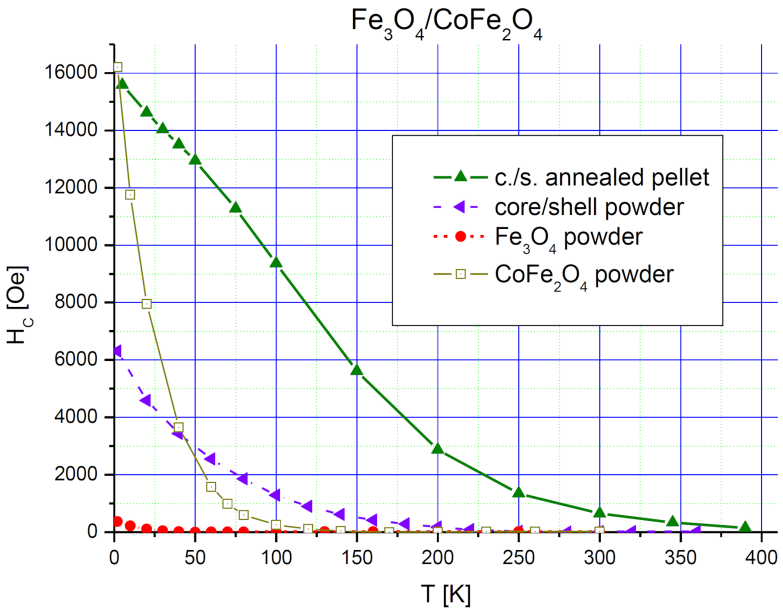

Fig. 7. Temperature dependences of coercive field H_c for as-prepared Fe_3O_4 nanoparticles, $Fe_3O_4/CoFe_2O_4$ (core–shell) nanoparticles, and annealed pellet (obtained by cold pressing) of $Fe_3O_4/CoFe_2O_4$ nanoparticles. The dependence for as-prepared $CoFe_2O_4$ particles (□) with diameters similar to those of Fe_3O_4 particles is presented for comparison[†1].

the shell to the nanoparticle characteristics, as well as by the modification of the core–shell interface parameters, as postulated in the work on similar nanoparticles (however, mostly coated with oleic acid and prepared mainly for biomedical applications) [45, 46]. Additionally, a kink in the magnetization curve is observed as the field approaches zero, which is characteristic of soft/hard nanostructures with a small part of the uncoupled soft phase.

The hysteresis loop for annealed pellets is smooth (implying coherent switching of spins in the efficiently exchange-coupled heterostructure), but with the coercivity almost three times higher than that for the powder. This increase in coercivity can be ascribed to the partial fusing of $CoFe_2O_4$ shells and the subsequent enhancement of magnetic interactions between neighboring nanoparticles (which can be treated as randomly oriented complex nanocrystallites), but also to the possible formation of an interdiffusion layer between the core and shells and/or other microstructural changes during annealing. The situation is additionally complicated by magnetoelastic contributions, because cobalt ferrite is a magnetostrictive material [47].

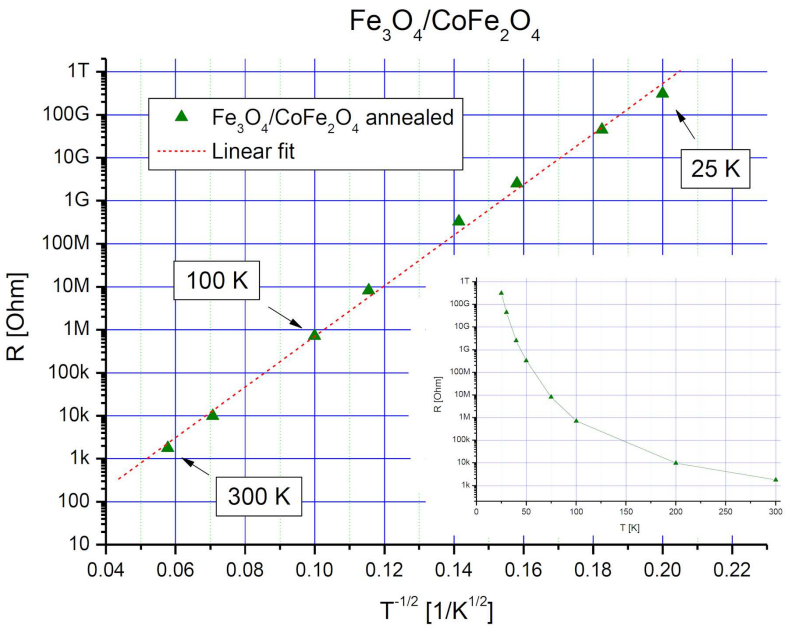

Fig. 8. Temperature dependence of the resistance of a compacted and annealed pellet of $Fe_3O_4/CoFe_2O_4$ nanoparticles plotted in $\log(R)$ vs $T^{-1/2}$ coordinates. The inset shows the same relationship plotted as $\log(R)$ versus T.

It is worth mentioning the observed substantial increase in the near-saturation magnetization after annealing, which correlates with the postulated (in Sect. 3.1) higher crystallinity index of the annealed sample.

Temperature dependences of the coercivity for the as-prepared Fe_3O_4 nanoparticles, $Fe_3O_4/CoFe_2O_4$ nanoparticles, and annealed pellet (obtained by cold pressing) of $Fe_3O_4/CoFe_2O_4$ particles are shown in Fig. 7. The dependence for as-prepared $CoFe_2O_4$ particles with diameters similar to those of Fe_3O_4 particles is also presented for comparison[†1]. It can be seen that the coercivity is higher for the as-prepared $Fe_3O_4/CoFe_2O_4$ nanoparticles studied in this work than for those studied in [23], which is due to the smaller diameter of the core, in agreement with the prediction that in a soft/hard granular system, H_c is inversely proportional to the size of the soft phase [48] as well as the thicker layer of the hard phase [49]. As seen in Fig. 7, the coercivity decreases monotonically with temperature for both samples, but for the as-prepared particles, it vanishes at a lower temperature, in correlation with the "blocking temperature".

The measured magnetic properties of $Fe_3O_4/CoFe_2O_4$ nanoparticles confirm the efficient core–shell exchange coupling (coherent switching of spins). In turn, for annealed pellets, we still have an efficiently exchange-coupled heterostructure, but there is also strong interparticle coupling (magnetic interactions between neighboring nanoparticles). Because heterostructured core–shell particles were grown individually, we can expect randomly oriented crystallographic axes (like in polycrystals). In an ideal case (thick shell), dominating $CoFe_2O_4$ magnetocrystalline anisotropy (with a large positive constant K in the bulk case) implies cubic easy axes [50] for the shell and, because of strong exchange coupling, can force the same (or similar) "effective" axes also for the entire particle. On the other hand, if the shell is exchange-coupled with the shells of adjacent particles, then there is a competition between the local anisotropies (possible random anisotropy effects [24]), the interconnecting couplings (exchange, dipolar), and the magnetoelastic interactions [47].

3.3. Resistivity

The resistivity, measured in the annealed pellet of $Fe_3O_4/CoFe_2O_4$ nanoparticles, is much higher than that expected for bulk Fe_3O_4 or $CoFe_2O_4$ spinels, which can be attributed to the increased contribution of contact resistances between nanoparticles due to their low dimensions. The fast decrease in the resistance with increasing temperature is characteristic of insulators, for which the concentration of charge carriers depends strongly on temperature. The thermal dependence of the resistance is close to linear when plotted in $\log(R)$ vs $T^{-1/2}$ coordinates (see Fig. 8).

The fact that resistivity is approximately proportional to $\exp[1/\sqrt{T}]$ suggests a vital role of a grain boundary tunneling conductance mechanism [51, 52]. This can be expected for a granular

system in which tunneling occurring through grain boundaries separating adjacent grains is the main contribution to resistivity [25, 53–55].

4. Conclusions

The structural, magnetic, and electric properties of cold-pressed and sintered $Fe_3O_4/CoFe_2O_4$ core–shell nanoparticle powder have been studied. The obtained hetero-structured magnetically soft/hard particles, several nanometers in diameter (synthesized by chemical co-precipitation), have the desired spinel-type structure and a relatively narrow size distribution. The complementary X-ray, EDX, and TEM results confirm the existence of a shell in the case of core–shell particles.

The efficient core–shell exchange coupling leads to a large increase in effective magnetic anisotropy. The coercive field (H_c) of the core–shell nanoparticles is much higher than that of magnetite. In the case of pellets (prepared by cold pressing and annealing), H_c increases much more because of stronger interparticle coupling and possible microstructural changes at the core–shell interfaces of the nanoparticles.

Preliminary electric measurements show an increased contribution of contact resistances between nanoparticles and suggest a vital role of a grain boundary tunneling conductance mechanism. More results (e.g., magnetoresistance data) and a detailed analysis of magnetic and electric transport properties will be presented in a separate work.

Acknowledgments

This work was performed within the collaborative project between the Polish and Ukrainian Academies of Sciences in laboratories co-financed by the ERDF Projects POIG.02.02.00-00-025/09 and POIG.02.01-00- 14-032/08. K.M. Kosyl acknowledges the support of the French Government Scholarship (BGF) program for the joint PhD thesis of the French Embassy in Poland.

References

[1] J.-B. Moussy, *J. Phys. D Appl. Phys.* **46**, 143001 (2013).

[2] R. von Helmolt, J. Wecker, B. Holzapfel, L. Schultz, K. Samwer, *Phys. Rev. Lett.* **71**, 2331 (1993).

[3] J.S. Moodera, L.R. Kinder, T.M. Wong, R. Meservey, *Phys. Rev. Lett.* **74**, 3273 (1995).

[4] G.-X. Miao, M. Munzenberg, J.S. Moodera, *Rep. Prog. Phys.* **74**, 036501 (2011).

[5] B. Dieny, V.S. Speriosu, S.S.P. Parkin, B.A. Gurney, D.R. Wilhoit, D. Mauri, *Phys. Rev. B* **43**, 1297(R) (1991).

[6] S. Yuasa, T. Nagahama, A. Fukushima, Y. Suzuki, K. Ando, *Nat. Mater.* **3**, 868 (2004).

[7] D.D. Djayaprawira, K. Tsunekawa, M. Nagai, H. Maehara, S. Yamagata, N. Watanabe, S. Yuasa, Y. Suzuki, K. Ando, *Appl. Phys. Lett.* **86**, 092502 (2005).

[8] F. Fabris, E. Lima Jr., C. Quinteros et al., *Phys. Rev. Appl.* **11**, 054089 (2019).

[9] R.A. de Groot, F.M. Mueller, P.G. van Engen, K.H.J. Buschow, *Phys. Rev. Lett.* **50**, 2024 (1983).

[10] W.E. Pickett, J.S. Moodera, *Phys. Today* **54**, 39 (2001).

[11] H.C. Kandpal, G.H. Fecher, C. Felser, *J. Phys. D Appl. Phys.* **40**, 1507 (2007).

[12] J.M.D. Coey, A.E. Berkowitz, Ll. Balcells, F.F. Putris, A. Barry, *Phys. Rev. Lett.* **80**, 3815 (1998).

[13] J.M.D. Coey, A.E. Berkowitz, Ll. Balcells, F.F. Putris, F.T. Parker, *Appl. Phys. Lett.* **72**, 734 (1998).

[14] J.M.D. Coey, *J. Appl. Phys.* **85**, 5576 (1999).

[15] X.W. Li, A. Gupta, G. Xiao, G.Q. Gong, *Appl. Phys. Lett.* **71**, 1124 (1997).

[16] H.Y. Hwang, S.W. Cheong, N.P. Ong, B. Batlogg, *Phys. Rev. Lett.* **77**, 2041 (1996).

[17] A.E. Berkowitz, J.R. Mitchell, M.J. Carey, A.P. Young, S. Zhang, F.E. Spada, F.T. Parker, A. Hutten, G. Thomas, *Phys. Rev. Lett.* **68**, 3745 (1992).

[18] J.Q. Xiao, J.S. Jiang, C.L. Chien, *Phys. Rev. Lett.* **68**, 3749 (1992).

[19] B.H. Zhou, J.D. Rinehart, *ACS Cent. Sci.* **4**, 1222 (2018).

[20] D.D. Sarma, S. Ray, K. Tanaka, M. Kobayashi, A. Fujimori, P. Sanyal, H.R. Krishnamurthy, C. Dasgupta, *Phys. Rev. Lett.* **98**, 157205 (2007).

[21] S. Jana, S. Middey, S. Ray, *J. Phys. Condens. Matter.* **22**, 346004 (2010).

[22] S. Ray, S. Middey, S. Jana, A. Banerjee, P. Sanyal, R. Rawat, L. Gregoratti, D.D. Sarma, *Europhys. Lett.* **94**, 47007 (2011).

[23] P.A. Kumar, S. Ray, S. Chakraverty, D.D. Sarma, *Appl. Phys. Lett.* **103**, 102406 (2013).

[24] A. López-Ortega, M. Estrader, G. Salazar-Alvarez, A.G. Roca, J. Nogues, *Phys. Rep.* **553**, 1 (2015).

[25] H. Liu, E.Y. Jiang, H.L. Bai, R.K. Zheng, H.L. Wei, X.X. Zhang, *Appl. Phys. Lett.* **83**, 3531 (2003).

[26] M. Fonin, Y. Dedkov, C. Konig, G. Guntherodt, U. Rudiger, J. Mayer, D. Vyalikh, S. Molodtsov, in: *Advances in Solid State Physics*, Vol. 43, Ed. B. Kramer, Springer, Berlin 2003, p. 487.

[27] A.V. Ramos, M.J. Guittet, J.B. Moussy, R. Mattana, C. Deranlot, F. Petroff, C. Gatel, *Appl. Phys. Lett.* **91**, 122107 (2007).

[28] S. Matzen, J.B. Moussy, R. Mattana, K. Bouzehouane, C. Deranlot, F. Petroff, *Appl. Phys. Lett.* **101**, 042409 (2012).

[29] A.V. Ramos, T.S. Santos, G.X. Miao, M.J. Guittet, J.B. Moussy, J.S. Moodera, *Phys. Rev. B* **78**, 180402(R) (2008).

[30] R.H. Kodama, *J. Magn. Magn. Mater.* **200**, 359 (1999).

[31] A. Houbi, Z.A. Aldashevich, Y. Atassi, Z.B. Telmanovna, M. Saule, K. Kubanych, *J. Magn. Magn. Mater.* **529**, 167839 (2021).

[32] Z. Ma, J. Mohapatra, K. Wei, J.P. Liu, S. Sun, *Chem. Rev.* **123**, 3904 (2023).

[33] A. Mitra, J. Mohapatra, M. Aslam, *Mater. Res. Express* **11**, 022002 (2024).

[34] Ö. Özdemir, *Geophys. J. Int.* **141**, 351 (2000).

[35] O.V. Yelenich, S.O. Solopan, J.M. Greneche, A.G. Belous, *Solid State Sci.* **46**, 19 (2015).

[36] F. Bosi, U. Halenius, H. Skogby, *Am. Mineral.* **94**, 181 (2009).

[37] H.-S. Shin, *J. Korean Ceram. Soc.* **35**, 1113 (1998).

[38] T.A.S. Ferreira, J.C. Waerenborgh, M.H.R.M. Mendonca, M.R. Nunes, F.M. Costa, *Solid State Sci.* **5**, 383 (2003).

[39] R. Frison, G. Cernuto, A. Cervellino, O. Zaharko, G.M. Colonna, A. Guagliardi, N. Masciocchi, *Chem. Mater.* **25**, 4820 (2013).

[40] A. Cervellino, R. Frison, G. Cernuto, A. Guagliardi, N. Masciocchi, *J. Appl. Cryst.* **47**, 1755 (2014).

[41] Q. Song, Z.J. Zhang, *J. Am. Chem. Soc.* **134**, 10182 (2012).

[42] O. Masala, D. Hoffman, N. Sundaram, K. Page, T. Proffen, G. Lawes, R. Seshadri, *Solid State Sci.* **8**, 1015 (2006).

[43] B. Issa, I.M. Obaidat, B.A. Albiss, Y. Haik, *Int. J. Mol. Sci.* **14**, 21266 (2013).

[44] A.H. Lu, E.L. Salabas, F. Schüth, *Angew. Chem. Int. Ed.* **46**, 1222 (2007).

[45] S.O. Solopan, N. Nedelko, S. Lewińska, A. Ślawska-Waniewska, V.O. Zamorskyi, A.I. Tovstolytkin, A.G. Belous, *J. Alloys Compd.* **788**, 1203 (2019).

[46] D. Polishchuk, N. Nedelko, S. Solopan, A. Ślawska-Waniewska, V. Zamorskyi, A. Tovstolytkin, A. Belous, *Nanoscale Res. Lett.* **13**, 67 (2018).

[47] E. du Tremolet de Lacheisserie, *Magnetostriction: Theory and Applications of Magnetoelasticity*, CRC Press, Boca Raton (FL) 1993.

[48] A. López-Ortega, M. Estrader, G. Salazar-Alvarez et al., *Nanoscale* **4**, 5138 (2012).

[49] G. Salazar-Alvarez, J. Sort, A. Uheida, M. Muhammed, S. Surinach, M.D. Baro, J. Nogues, *J. Mater. Chem.* **17**, 322 (2007).

[50] J.M.D. Coey, *Magnetism and Magnetic Materials*, Cambridge University Press, Cambridge 2010.

[51] P. Sheng, *Philos. Mag. B* **65**, 357 (1992).

[52] P. Sheng, *Phys. Rev. B* **21**, 2180 (1980).

[53] C. Park, Y. Peng, J.G. Zhu, D.E. Laughlin, R.M. White, *J. Appl. Phys.* **97**, 10C303 (2005).

[54] P. Sheng, B. Abeles, Y. Arie, *Phys. Rev. Lett.* **31**, 44 (1973).

[55] H. Liu, E.Y. Jiang, H.L. Bai, R.K. Zheng, X.X. Zhang, *J. Phys. D Appl. Phys.* **36**, 2950 (2003).